**Biophysical Journal, Volume *120***

## Supplemental Information

# Computational Tool for Ensemble Averaging of Single-Molecule Data

**Thomas Blackwell, W. Tom Stump, Sarah R. Clippinger, and Michael J. Greenberg**

# Supporting Materials

## Computational Tool for Ensemble Averaging of Single-Molecule Data

Thomas Blackwell[1], W. Tom Stump[1], Sarah R. Clippinger[1], Michael J. Greenberg[1]
[1]Department of Biochemistry and Molecular Biophysics, Washington University School of Medicine, St. Louis, MO, 63110, USA

## Supplemental Materials and Methods

*Implementation of the computational tool*

The SPASM computational tool, which includes a graphical user interface, was written in MATLAB (MathWorks). The program uses the Signal Processing Toolbox and the Optimization Toolbox, but neither toolbox is required for analysis. The code was tested on MATLAB versions R2017b through R2020a for both Windows and macOS operating systems. Standalone versions of the program for both Windows and macOS were generated using the MATLAB Compiler.

The SPASM computational tool can be found at: https://github.com/GreenbergLab/SPASM. This repository includes the open source code for SPASM (**SPASM.m**), compiled versions for Windows (**SPASM_Windows.exe**) and macOS (**SPASM_macOS.app.zip**), a versions of the program which analyze only one trapped bead and uses variance thresholds rather than covariance thresholds (**SPASM_one_bead.m, SPASM_one_bead_Windows.exe, SPASM_one_bead_macOS.app.zip**), MATLAB code to generate simulated data (**simulator.m**), a user guide for the aforementioned components (**SPASM_user_guide.pdf**), and the simulated data sets analyzed in this paper (**sets 1-30**).

*Detection of binding interactions*

Binding interactions between a motor and its track in the optical trap can be identified using either a variance (1) or a covariance (2, 3) threshold, since the binding of a motor to its track causes a reduction in both the variance and covariance of the two beads (**Fig. 2**). The covariance between the beads at any time, t, is calculated by:

$$\mathrm{Cov}_t(A, B) = \mathrm{E}_{w_c,t}[A * B] - \mathrm{E}_{w_c,t}[A] * \mathrm{E}_{w_c,t}[B]$$

where A is the position of one bead (bead A), B is the position of the other bead (bead B), and $\mathrm{E}_{w_c,t}[X]$ denotes the mean of X over a window of size $w_c$ centered at t. Before generating a histogram of covariance values, the covariance is smoothed using a second-order Savitzky-Golay filter with window size $w_s$ to remove high-frequency noise. The values of $w_c$ and $w_s$ can be optimized using the computational tool. See the Supporting Materials for details.

A histogram of the filtered covariance between the two beads shows two distinct populations corresponding to bound (B) and unbound (U) states (**Fig. 2**). This histogram can be used to determine covariance thresholds for detecting binding interactions (4). We use one of two methods to detect binding interactions from the covariance: (1) assigning a single threshold based on the minimum value between the covariance peaks or (2) using a peak-to-peak method which requires that the covariance extend between the bound peak and the unbound peak. The advantages and disadvantages of these methods are discussed in detail in the Results and Discussion.

Once potential binding interactions have been identified, temporal thresholds can be applied to filter the interactions. Any observed reductions in the covariance which are

shorter than a user-defined minimum duration are ignored to lower the chance of mistakenly identifying random correlated noise as a binding interaction. Also, any two binding interactions which are separated in time by less than a user-defined minimum separation are ignored to lower the chance of mistakenly identifying random noise as premature detachment between the motor and the track. Note that this filtering takes place after the change points have been located.

*Binding interaction alignment using a change point algorithm and the generation of ensemble averages*

Constructing ensemble averages requires the synchronization of individual binding interactions at transitions between the bound and unbound states. Here, we implement a change point algorithm to identify transitions. This algorithm uses maximum likelihood estimation to locate the times, or change points, where changes in both the mean and variance of each bead's position have most likely occurred. For each binding interaction identified using covariance thresholds, the algorithm searches for the change points within a window of data. For the $k^{th}$ binding interaction, this window spans from

$$t_1 = t_{k,start} - 0.49 * \min\left(t_{k,end} - t_{k,start}, t_{k,start} - t_{k-1,end}\right)$$

to

$$t_N = t_{k,end} + 0.49 * \min\left(t_{k,end} - t_{k,start}, t_{k+1,start} - t_{k,end}\right)$$

where $t_{k,start}$ and $t_{k,end}$ denote the beginning and end times of the $k^{th}$ interaction as estimated by the covariance threshold method. The window must be wide enough that it includes the entirety of the $k^{th}$ interaction but not so wide that it contains part of another interaction. The computational tool automatically searches the default window for change

points, but it also allows for manual adjustment of both the search window and the identified change points.

The algorithm considers the average position between beads A and B during this window. For each pair of time points within the window, $(t_i, t_j)$, the algorithm calculates the likelihood that these points coincide with changes in the mean and variance of the data. Each pair divides the window into three intervals: $[t_1, t_i]$, $[t_{i+1}, t_j]$, and $[t_{j+1}, t_N]$, where $1 < i < j < N$. The log-likelihood score, $L_{(t_i,t_j)}$, assigned to $(t_i, t_j)$ measures how well normal distributions can be fit to these intervals of data:

$$L_{(t_i,t_j)} = -\left[\frac{j-i}{2}\ln\left(\sigma^2{}_{[t_{i+1},t_j]}\right)\right] - \left[\frac{N-j+i}{2}\ln\left(\sigma^2{}_{[t_1,t_i]\cup[t_{j+1},t_N]}\right)\right]$$

where $\sigma^2$ is the variance of the data during the corresponding interval (see the Supporting Materials for the derivation). $L$ is maximized where the values of $t_i$ and $t_j$ best divide the window into three sequences of normally distributed data, and these values of $t_i$ and $t_j$ are then assigned as the change points.

After synchronization at the change points, both time forward and time reversed ensemble averages of individual binding interactions are generated from the average of the two beads' positions using well-established methods (5). Shorter-lived binding interactions are extended in time to match the duration of the longest-lived binding interaction. The value of this extension equals the average position of the beads during either the first or last 5 ms of the binding interaction for the time reversed and time forward averages, respectively.

*Generation of simulated single-molecule data*

To test the accuracy of the program and to aid in the selection of proper window sizes for the analysis of experimental data, we created an additional program to simulate data that resembles single-molecule interactions collected using our optical trapping system with user-defined substep sizes and kinetics. It is important to note that the signal-to-noise ratio will vary between instruments. The code for this program is provided alongside SPASM so that users can adapt the simulation parameters for their system of interest. Rather than explicitly solving the equations of motion for the optically trapped beads, the parameters used for simulation can be empirically varied until the simulated data matches the experimental data. Trapping data is simulated using a continuous-time Markov jump process in which the motor switches among a baseline detached state and two successive attached states, each with a unique displacement, representing a motor with a two-substep working stroke. The user can set the number of states, the rates of transitioning between the states, and the displacements of each state. High-frequency Gaussian noise is added to simulate Brownian motion. To simulate mechanical coupling between the beads (i.e., higher covariance), a fraction of the noise in each bead's position, $f$, is shared between the two beads. When the motor is dissociated from its track, $f$ is set to a larger number so that the motion of the two beads is correlated. When the motor is bound to the track, $f$ is set to a lower number, resulting in a lower covariance. Drift in the system is simulated by the addition of low-frequency noise. For additional details, see the Supporting Materials and the provided code.

*Analysis of simulated data*

To test our analysis approach, we generated simulations with well-defined characteristics. Data were simulated with a 2 kHz sampling rate. First, we generated 10 data sets (sets 1-10), each containing 100 binding interactions, to simulate beta cardiac myosin based on previous optical trapping and kinetic measurements (6-8). The rate of transitioning from the detached state to the first attached state was set to 0.5 $s^{-1}$. The rate of transitioning from the first attached state to the second attached state was set to 70 $s^{-1}$, matching the rate of ADP release (9). The rate of transitioning from the second attached state to the detached state was 4 $s^{-1}$, matching the rate of ATP-induced actomyosin dissociation at 1 μM ATP. The myosin was modeled to have a two-substep working stroke with a 4.7 nm substep followed by a second substep of 1.9 nm (6).

We then generated 10 more data sets to analyze with SPASM (sets 11-20). Each of these sets of data contained 100 simulated binding interactions. The rate of transitioning from the detached state to the first attached state remained at 0.5 $s^{-1}$. The rate of transitioning from the first attached state to the second attached state, however, was much lower at 5 $s^{-1}$, and the rate of transitioning from the second attached state to the detached state was 2 $s^{-1}$. As before, the myosin was modeled to have a two-substep working stroke with a 4.7 nm substep followed by a second substep of 1.9 nm.

With the simulated data, the exact locations of transition points between the bound and unbound states are known, allowing us to test the performance of different analysis methods with regards to: (1) the frequency of false positive binding interactions (i.e., when the bound state is incorrectly detected while the motor is actually unbound), (2) the number of false negative binding interactions (i.e., when the unbound state is incorrectly

detected while the motor is actually bound), and (3) the error in determining the correct initiation and termination times of each binding interaction.

To determine the number of false positives, each detected binding interaction was mapped to the nearest overlapping real binding interaction. If a detected binding interaction did not overlap with any real binding interactions, it was counted as a false positive. If multiple detected binding interactions were mapped to the same real binding interaction, all but the closest were also counted as false positives. As we fixed the number of simulated binding interactions within each data set, rather than the total duration of each data set, the data sets typically varied in duration. A longer set of data is expected to result in more false positives, and so the frequency of false positives was calculated by dividing the number of false positives by the duration of the data set. To determine the number of false negatives, each real binding interaction was mapped to the nearest overlapping detected binding interaction. If a real binding interaction did not overlap with any detected binding interactions, it was counted as a false negative. If multiple real binding interactions were mapped to the same detected binding interaction, all but the closest were also counted as false negatives. The error was calculated as the difference between the computationally identified transition points and the nearest simulated transition points for which the corresponding binding interactions overlapped.

*Statistical analysis*

Simulated binding interactions were detected using either the single threshold method or the peak-to-peak method (3), and the frequency of false positives and the number of false negatives were determined. To test for a significant difference in the mean

frequency of false positives or the mean number of false negatives between the two methods, p-values were obtained from the independent two-sample t-test. To test if the median error of the detected transition points was significantly changed with the addition of the change point algorithm, p-values were obtained from the Wilcoxon rank sum test.

Ensemble averages were generated from each method of analysis, as well as from the known locations of actual simulated binding interactions. To extract parameters from the ensemble averages, exponential curves were fit to each average, yielding estimates for the substep sizes and rates of the simulated data. For each extracted parameter, a Kruskal-Wallis test was used followed by pairwise Wilcoxon rank sum tests to determine p-values.

*Design of optical trapping apparatus*

Experiments were performed on a custom-built, microscope free dual beam optical trap, based on (10, 11). The optical layout is described in the Supporting Materials and Methods (**Fig. S1**). Briefly, the output from a 10 W 1064 nm laser beams (IPG Photonics) was rotated by 45 degrees and then separated into vertically and horizontally polarized components to form 2 independent traps. Optical traps were independently steerable using acoustic optical deflectors (Gooch and Housego) and frequency synthesizer boards under FPGA control (Analog Devices, AD9910 Direct Digital Synthesis evaluation boards). The light from the trapping laser was used for determining the displacement of the beads from the center of the optical trap, and this was measured at the back focal plane using two quadrant photodiodes (501104, First Sensor). Data were low pass filtered (Frequency Devices) to the Nyquist frequency and digitized on a National Instruments

FPGA board (PCIe 7852) with simultaneously sampling analog to digital converters. System control was accomplished by custom software written in LabView. 3D stage control was achieved using a piezoelectric stage (Mad City Labs). Fluorescence was illuminated using the output of a 50 mW 532 laser (Crystalaser). Imaging was performed using an EMCCD camera (Andor).

*Optical trapping experiments*

Porcine cardiac myosin and actin were purified from cryoground tissue (Pelfreez) as previously described (12, 13). Bead coated flow cells were assembled as previously described (3, 6, 14). All experiments were performed in KMg25 buffer (60 mM MOPS pH 7.0, 25 mM KCl, 2 mM EGTA, 4 mM $MgCl_2$, 1 mM DTT). All buffers and dilutions were prepared fresh each day. Biotin-labeled actin (2 μM) was prepared using 10% biotin actin (Cytoskeleton) in KMg25 buffer. The mixture was allowed to polymerize for 20 minutes, and then the actin was stabilized using tetramethylrhodamine isothiocyanate-labeled phalloidin. 1 μm diameter, polystyrene beads coated with streptavidin (Bangs Labs) were washed in 1 mg/mL BSA in KMg25 buffer three times. Flow cells were loaded with myosin (4-20 nM in KMg25 with 200 mM KCl) for 5 minutes and then blocked with 1 mg/mL BSA for 5 minutes. Activation buffer contained KMg25 with the addition of 1 μM ATP, 192 U/mL glucose oxidase, 48 μg/mL catalase, 1 mg/mL glucose, and ~25 pM Biotin rhodamine-phalloidin actin. A small amount (4 μL) of streptavidin beads were loaded into the flow cell, and the flow cell was sealed with vacuum grease. Trapping experiments were conducted as previously described (3). Two streptavidin beads were optically trapped, forming a bead-actin-bead dumbbell. Trap stiffness was determined by fitting of the power

spectral density collected at 20 kHz. The bead-actin-bead dumbbell was pretensed to approximately 2-3 pN and then lowered onto a surface bead to search for binding interactions. Approximately 1 in 5 beads showed binding interactions. Data were acquired at 2 kHz and filtered to 1 kHz.

**Derivation of the log-likelihood function for the change point algorithm**

Generally, given a set of data, a change point algorithm can help determine whether any changes have occurred and, if so, where the changes most likely occurred. In our implementation, we first use the covariance to identify binding interactions and then apply the change point algorithm to precisely determine where the transitions between the bound and unbound states occurred. For each identified binding interaction, we consider windows of data surrounding the interactions. Therefore, we assume each window contains exactly two change points, and we only need to determine where they occur.

The change point algorithm aims to maximize the log-likelihood function, whose derivation requires knowledge of the distributions underlying a particular set of data. In the case of optical trapping data, the data points are typically normally distributed with unique means and variances for the bound and unbound states. Other types of data sets might have different underlying distributions and therefore different log-likelihood functions that must be maximized. For example, in the case of single molecule FRET data, the distributions of FRET efficiencies in each state typically have unique means but do not necessarily have unique variances. In the case of single photon wait times, the underlying distributions are Poisson distributed rather than normally distributed. Below, we show how to derive the log-likelihood function for normally distributed data with a change in both mean and variance, using maximum likelihood estimation. For other types of data, the log-likelihood function can be derived using similar methods.

For a window of data occurring at times $\boldsymbol{T} = \{1,2, \dots, N\}$, we know the average position of the beads $\boldsymbol{X} = \{X_1, X_2, \dots, X_N\}$. We assume there exist times $i$ and $j$ within

$\{1,2,\dots,N-1\}$ such that $\{X_1, X_2, \dots, X_i\}$ and $\{X_{j+1}, X_{j+2}, \dots, X_N\}$ are drawn from some normal distribution $N(\mu_U, {\sigma_U}^2)$ and $\{X_{i+1}, X_{i+2}, \dots, X_j\}$ are drawn from a second normal distribution $N(\mu_B, {\sigma_B}^2)$. Therefore, the density function for any point $X_k$ within our data is:

$$f(X_k) = \begin{cases} \frac{1}{\sqrt{2\pi{\sigma_U}^2}} \exp\left[-\frac{1}{2}\left(\frac{X_k - \mu_U}{\sigma_U}\right)^2\right], & \text{if } 1 \le k \le i \text{ or } j < k \le N \\ \frac{1}{\sqrt{2\pi{\sigma_B}^2}} \exp\left[-\frac{1}{2}\left(\frac{X_k - \mu_B}{\sigma_B}\right)^2\right], & \text{if } i < k \le j \end{cases}$$

Assuming independence among the datapoints, the probability of obtaining the entire data set $\boldsymbol{X}$ is given by the likelihood function:

$$f(\boldsymbol{X}) = f(X_1)f(X_2)\dots f(X_N)$$

$$= \left(\prod_{k=1}^{i} \frac{1}{\sqrt{2\pi{\sigma_U}^2}} \exp\left[-\frac{1}{2}\left(\frac{X_k - \mu_U}{\sigma_U}\right)^2\right]\right) * \left(\prod_{k=i+1}^{j} \frac{1}{\sqrt{2\pi{\sigma_B}^2}} \exp\left[-\frac{1}{2}\left(\frac{X_k - \mu_B}{\sigma_B}\right)^2\right]\right)$$

$$* \left(\prod_{k=j+1}^{N} \frac{1}{\sqrt{2\pi{\sigma_U}^2}} \exp\left[-\frac{1}{2}\left(\frac{X_k - \mu_U}{\sigma_U}\right)^2\right]\right)$$

Only the values $\{X_1, X_2, \dots, X_N\}$ are known. We wish to determine values for the parameters $\mu_U$, ${\sigma_U}^2$, $\mu_B$, ${\sigma_B}^2$, $i$, and $j$ which maximize $f$. Equivalently, one could maximize the log-likelihood function. The log-likelihood function is the natural logarithm of $f$:

$$\ln f = \left[-\frac{i}{2}\ln(2\pi{\sigma_U}^2) - \frac{1}{2{\sigma_U}^2}\sum_{k=1}^{i}(X_k - \mu_U)^2\right]$$

$$+ \left[-\frac{j-i}{2}\ln(2\pi{\sigma_B}^2) - \frac{1}{2{\sigma_B}^2}\sum_{k=i+1}^{j}(X_k - \mu_B)^2\right]$$

$$+ \left[-\frac{N-j}{2}\ln(2\pi{\sigma_U}^2) - \frac{1}{2{\sigma_U}^2}\sum_{k=j+1}^{N}(X_k - \mu_U)^2\right]$$

An estimate for $\widehat{\mu_U}$, the value of $\mu_U$ which maximizes $\ln f$, is obtained by solving $\frac{\partial \ln f}{\partial \mu_U} = 0$:

$$\frac{\partial \ln f}{\partial \mu_U} = \frac{1}{{\sigma_U}^2}\left[\sum_{k=1}^{i}(X_k - \mu_U) + \sum_{k=j+1}^{N}(X_k - \mu_U)\right]$$

$$= \frac{1}{{\sigma_U}^2}\left[\left(\sum_{k=1}^{i} X_k + \sum_{k=j+1}^{N} X_k\right) - (N - j + i)\mu_U\right] = 0$$

$$\Rightarrow \sum_{k=1}^{i} X_k + \sum_{k=j+1}^{N} X_k = (N - j + i)\mu_U$$

$$\Rightarrow \widehat{\mu_U} = \frac{1}{(N - j + i)}\left[\sum_{k=1}^{i} X_k + \sum_{k=j+1}^{N} X_k\right]$$

The estimate for $\widehat{\mu_B}$ is found similarly to be:

$$\widehat{\mu_B} = \frac{1}{j - i}\sum_{k=i+1}^{j} X_k$$

An estimate for $\widehat{{\sigma_U}^2}$ is obtained by solving $\frac{\partial \ln f}{\partial {\sigma_U}^2} = 0$ and using $\widehat{\mu_U}$ as an estimate for $\mu_U$:

$$\frac{\partial \ln f}{\partial {\sigma_U}^2} = -\frac{N - j + i}{2{\sigma_U}^2} + \frac{1}{2{\sigma_U}^4}\left[\sum_{k=1}^{i}(X_k - \mu_U)^2 + \sum_{k=j+1}^{N}(X_k - \mu_U)^2\right] = 0$$

$$\Rightarrow \frac{N - j + i}{2{\sigma_U}^2} = \frac{1}{2{\sigma_U}^4}\left[\sum_{k=1}^{i}(X_k - \mu_U)^2 + \sum_{k=j+1}^{N}(X_k - \mu_U)^2\right]$$

$$\Rightarrow N - j + i = \frac{1}{{\sigma_U}^2}\left[\sum_{k=1}^{i}(X_k - \mu_U)^2 + \sum_{k=j+1}^{N}(X_k - \mu_U)^2\right]$$

$$\Rightarrow \widehat{{\sigma_U}^2} = \frac{1}{N - j + i}\left[\sum_{k=1}^{i}(X_k - \widehat{\mu_U})^2 + \sum_{k=j+1}^{N}(X_k - \widehat{\mu_U})^2\right]$$

The estimate for $\widehat{{\sigma_B}^2}$ is similarly given by:

$$\widehat{{\sigma_B}^2} = \frac{1}{j - i}\sum_{k=i+1}^{j}(X_k - \widehat{\mu_B})^2$$

The log-likelihood function simplifies after these values are substituted:

$$\ln f = \left[-\frac{j - i}{2}\ln\left(2\pi\widehat{{\sigma_B}^2}\right) - \frac{N - j + i}{2}\ln\left(2\pi\widehat{{\sigma_U}^2}\right)\right] - \frac{j - i}{2} - \frac{N - j + i}{2}$$

$$= \left[ -\frac{j-i}{2} \ln\left(\widehat{\sigma_B}^2\right) - \frac{N-j+i}{2} \ln\left(\widehat{\sigma_U}^2\right) \right] - \frac{N}{2} \ln(2\pi) - \frac{N}{2}$$

It is sufficient to maximize the following function:

$$L = -\frac{j-i}{2} \ln\left(\widehat{\sigma_B}^2\right) - \frac{N-j+i}{2} \ln\left(\widehat{\sigma_U}^2\right)$$

This function depends only on $\boldsymbol{X}$, $i$, and $j$. As $i$ and $j$ must be within the set $\{1,2,\dots,N-1\}$, $\hat{\imath}$ and $\hat{\jmath}$ may be determined empirically.

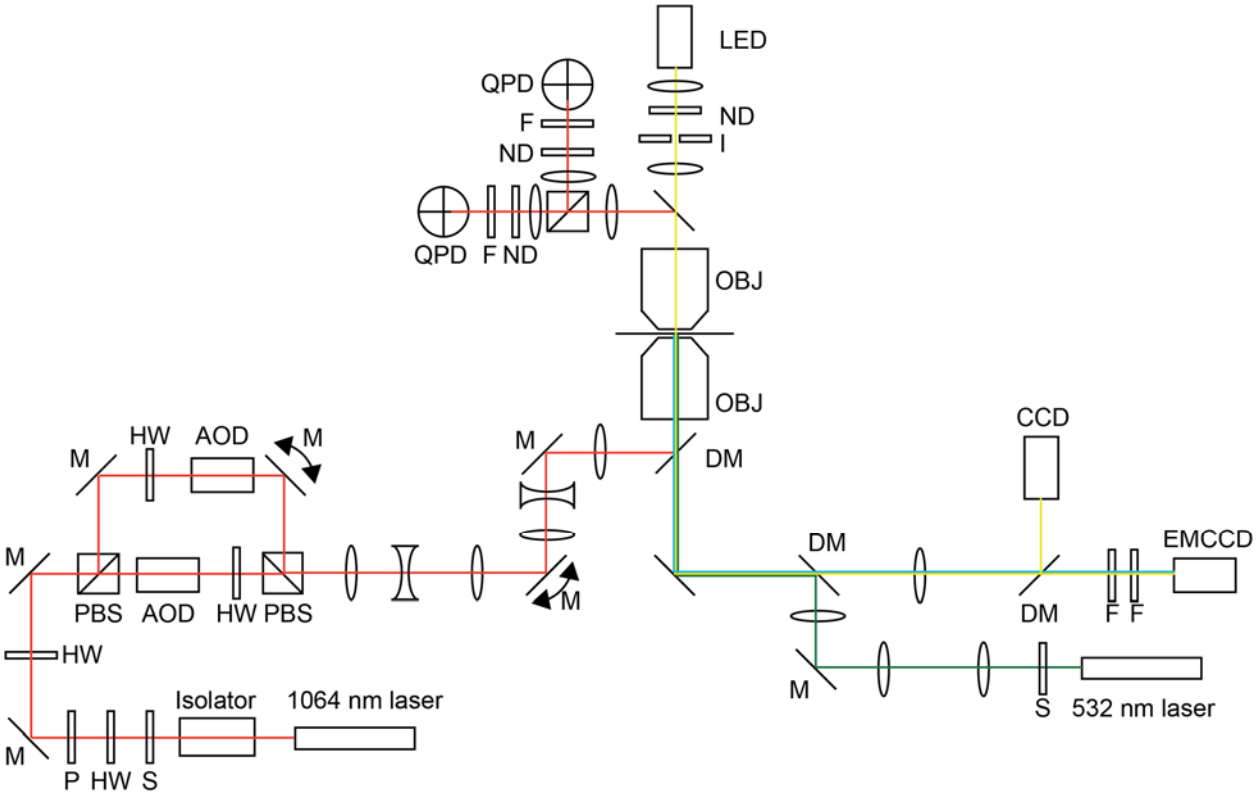


**Figure S1. Optical trap layout.** A half-wave plate (HW) / polarizer (P) combination attenuates the vertically polarized 1064 nm trapping laser beam (IPG) to the intensity required for the experiment, while a second half-wave plate adjusts the polarization angle to 45 degrees such that two traps with orthogonal polarization and equal power can be formed. The beam is split into vertical and horizontal components by the first polarizing beam splitter (PBS, Newport), and each beam passes through an acousto-optic deflector (AOD, Gooch and Housego) for computer-controlled trap steering and power control. The AODs require an input polarization parallel to their horizontal steering plane, and the output from the AODs is vertically polarized. Therefore, a half-wave plate is needed to rotate the polarization before one AOD, and a separate half-wave plate is used to rotate polarization after the other AOD. The two polarization separated beams are then recombined using a second PBS. The beams are then expanded to fill the back aperture

of the microscope objective by a pair of beam expanders, each formed by two planoconvex lenses with a biconcave lens at the crossover point to limit fluctuations caused by localized heating of the air. Motorized mirrors (M, with arrows, Newport) are placed at two points for coarse positioning of the beams: the first adjusts one trap's position while the second, which is conjugate to the back aperture of the objective, repositions both traps simultaneously in the microscope field of view. The AOD's and quadrant photodiode detectors (QPDs, see below) are conjugate to the back focal plane of the objective so that beam steering is not registered as signal change on the QPDs. After the laser beams pass through the trapped beads, the resulting interference patterns are collected by the condenser (a second objective lens) and split into their respective polarizations by a PBS. These polarization-separated interference patterns are then imaged onto the two quadrant photodiodes (QPDs, First Sensor). Neutral density (ND) and 1064 nm bandpass filters (F) are used to avoid detector saturation and to remove non-trapping wavelengths of light, respectively.

Beads are visualized on an electron multiplying charge coupled device (EMCCD), or alternatively a standard CCD camera using wide field transillumination provided by a 730 nm LED (Thorlabs). An iris (I) is positioned so that its image is in focus when the condenser is set at the correct height for trapping beam imaging onto the QPDs. Before reaching the condenser, this beam passes through a dichroic mirror (DM, Semrock) that is used to reflect the trapping beams to the QPDs.

The EMCCD is also used to visualize fluorescent actin molecules in a wide field epifluorescence arrangement using an expanded 532 nm laser (CrystaLaser) introduced into the trapping beam path with a dichroic mirror. Another dichroic mirror separates the

excitation light from the emission signal, which is subsequently filtered by dual filters (F). Both the 532 nm and 1064 nm lasers have shutters (S).

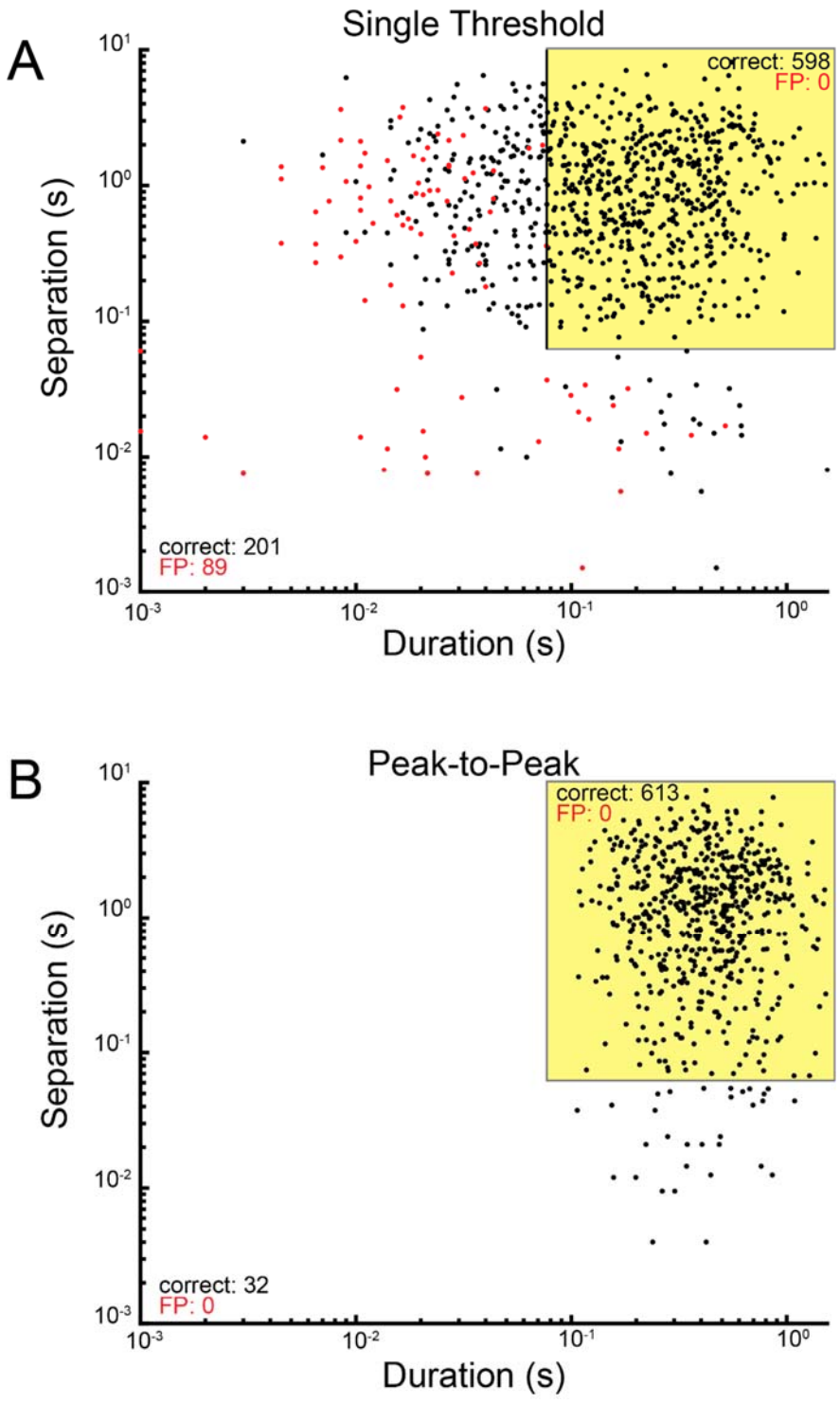


**Figure S2. The single threshold method detects more false positive binding interactions than the peak-to-peak method, and efficiently excluding these**

**interactions is difficult.** 10 sets of data, each containing 100 simulated binding interactions, were analyzed by either the single threshold method or the peak-to-peak method. (**A**) Scatter plot showing the duration and the smaller of the two separations of each binding interaction detected by the single threshold method, both in units of seconds. A binding interaction's two separations are the amounts of time separating that interaction from the preceding and subsequent interactions. Both axes are scaled logarithmically. False positive interactions identified by the method are shown in red. As can be seen, most false positive interactions have relatively short durations and/or separations. The yellow box indicates the binding interactions which remain after filtering out any interactions with a duration shorter than 77 ms or a separation shorter than 63 ms. These two values were chosen to be as small as possible while still filtering out all false positive interactions. Due to significant overlap between the false positive interactions and many of the correctly detected interactions, it is not easy to pick suitable values for filtering the interactions unless the false positive binding interactions have already been identified. This can only confidently be done using simulated data where one can know for certain whether a detected interaction is a false positive. After the filtering takes place, 598 interactions remain. (**B**) Scatter plot showing the duration and the smaller of the two separations of each binding interaction detected by the peak-to-peak method. No false positive interactions were detected by the peak-to-peak method. Applying the same filtering as with the single threshold method leaves 613 interactions. Note that the durations and separations are calculated based on the binding initiation and termination times estimated by the single threshold or peak-to-peak method. A binding interaction detected by the peak-to-peak method will always appear to be longer than the

corresponding interaction detected by the single threshold method (see main text for details).

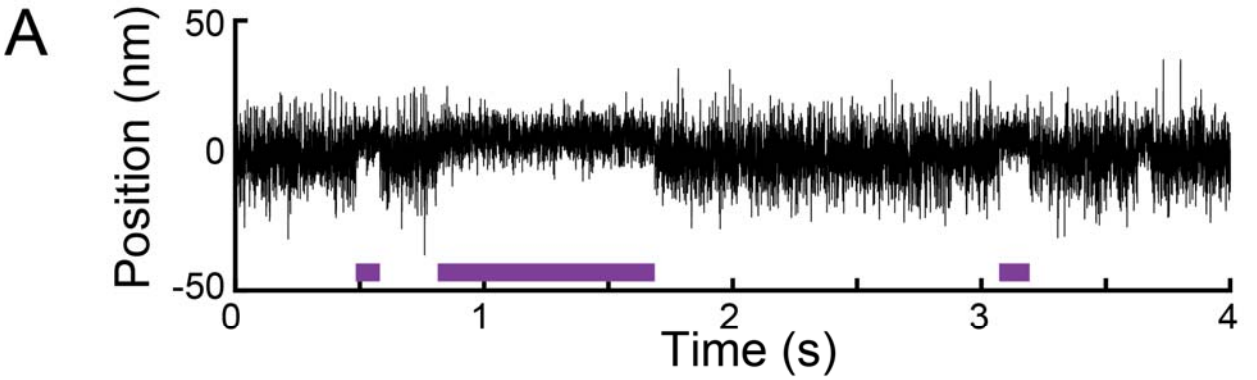


| Method | Average # of correctly detected interactions (mean ± SD) | Average # of missed interactions (mean ± SD) | # of false positive interactions / 100 seconds (mean ± SD) |
|---|---|---|---|
| Single threshold | 80 ± 4 | 20 ± 4 | 4 ± 1 |
| Peak-to-peak | 65 ± 5 | 36 ± 5 | 0 |

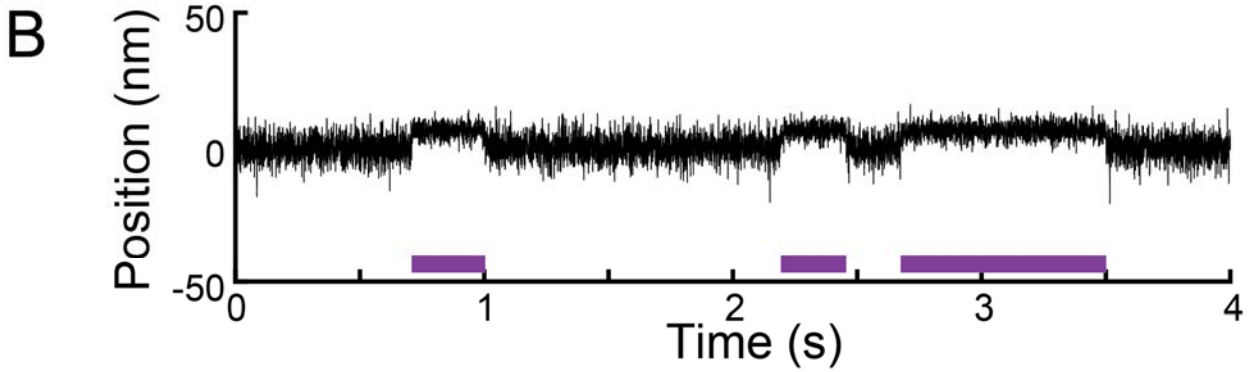


| Method | Average # of correctly detected interactions (mean ± SD) | Average # of missed interactions (mean ± SD) | # of false positive interactions / 100 seconds (mean ± SD) |
|---|---|---|---|
| Single threshold | 99 ± 1 | 2 ± 1 | 6 ± 2 |
| Peak-to-peak | 90 ± 3 | 10 ± 1 | 0.08 ± 0.16 |

**Figure S3. Higher signal-to-noise ratios enable the detection of a greater number of binding interactions, with fewer missed binding interactions.** 10 sets of data, each containing 100 simulated binding interactions, were analyzed by either the single threshold method or the peak-to-peak method. Purple bars show binding interactions identified using the peak-to-peak method. (**A**) Simulated data trace taken from data sets

1-10. This is the same data set analyzed in Table S1. (**B**) Simulated data trace with a greater signal-to-noise ratio, taken from data sets 21-30. The signal-to-noise ratio was increased in the simulations by reducing the amplitude of the high frequency noise. The increased signal-to-noise ratio enabled the detection of a greater number of binding interactions, with fewer binding interactions being missed.

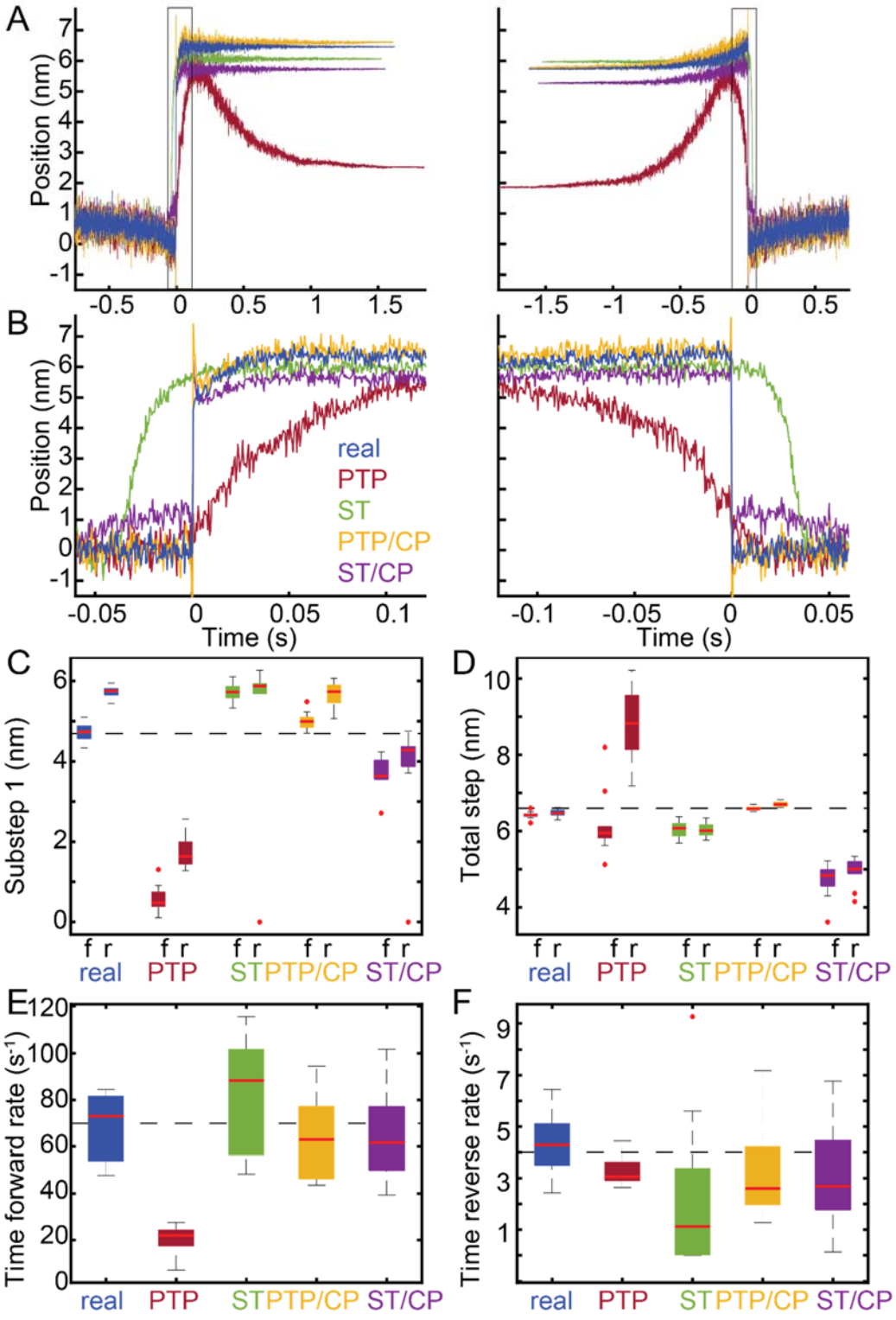
A
Position (nm)
B
Position (nm)
real
PTP
ST
PTP/CP
ST/CP
Time (s)
Time (s)
C
Substep 1 (nm)
D
Total step (nm)
f r
real
PTP
ST
PTP/CP
ST/CP
E
Time forward rate (s-1)
F
Time reverse rate (s-1)

**Figure S4. Ensemble averages generated with the single threshold method without filtering events leads to an underestimate of the total step size due to the inclusion of false positive binding interactions.** The same sets of simulated data were analyzed as with **Fig. 5** (sets 1-10), each containing 100 binding interactions. As with **Fig. 5**, interactions were detected using either the peak-to-peak (PTP) or the single threshold (ST) method, and interactions were aligned using either the transitions estimated by the covariance threshold method or the change points identified by the change point algorithm (CP). Here, unlike with **Fig. 5**, none of the binding interactions detected by the single threshold method were removed. Many of these binding interactions are false positives (see Figure S2). (**A-B**) Time forward (left) and time reversed (right) ensemble averages were generated from the known locations of the actual simulated binding interactions (real) and from each method of analysis. (**C-F**) Within each of the 10 sets of data, ensemble averages were generated and fit with single exponential functions. The substep sizes and rates of the simulated myosin working stroke were estimated from the exponential fits. Box plots show the estimated parameters for each analysis method. Outliers are indicated by red dots. The substep sizes were estimated from both the time forward (f) and time reversed (r) ensemble averages. Horizontal dashed lines show the values of the simulated parameters. The total step size is underestimated by the single threshold method, both with (ST/CP) and without (ST) the change point algorithm, due to the inclusion of false positive binding interactions which do not generate any net displacement in the optical trap.

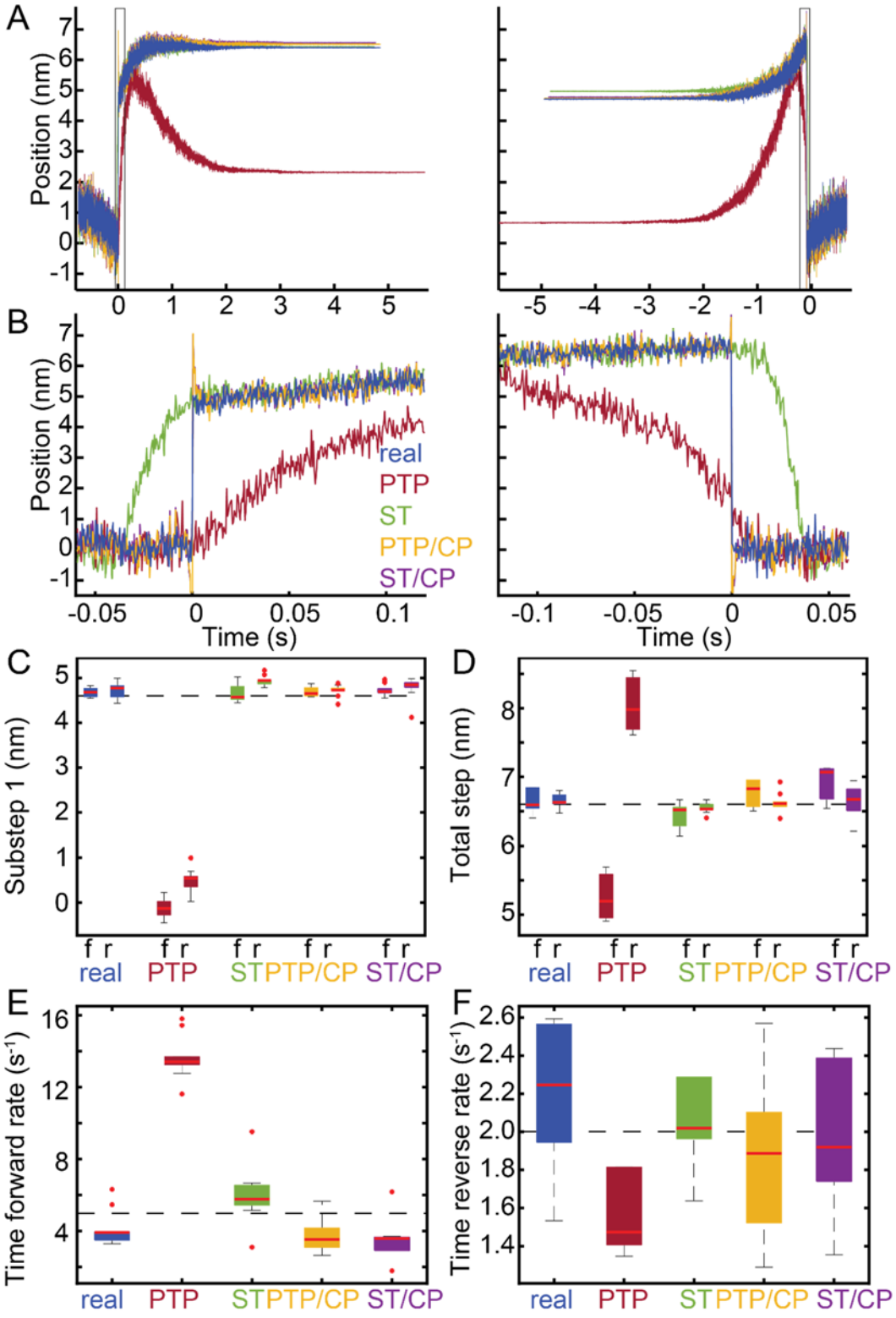


**Figure S5. Ensemble averages are able to accurately estimate the substep sizes and kinetic rates when the underlying transitions have slower kinetics.** 10 sets of

data were simulated, each containing 100 binding interactions (sets 11-20). Here, the rate of transitioning from the first to second substep was set to 5 $s^{-1}$, which is much lower than the rate of 70 $s^{-1}$ used in **Fig. 5**. Additionally, the rate of transitioning from the second substep to the detached state was set to 2 $s^{-1}$. The magnitude of the two substeps were still 4.7 nm and 1.9 nm, as before. As in **Fig. 5**, interactions were detected using either the peak-to-peak (PTP) or the single threshold (ST) method, and interactions were aligned using either the transitions estimated by the covariance threshold method or the change points identified by the change point algorithm (CP). Also similar to **Fig. 5**, binding interactions detected by the single threshold method which were too short or too close to other interactions were excluded from analysis, to minimize the number of false positive interactions. (**A-B**) Time forward (left) and time reversed (right) ensemble averages were generated from the known locations of the actual simulated binding interactions (real) and from each method of analysis. (**C-F**) Within each of the 10 sets of data, ensemble averages were generated and fit with single exponential functions. The substep sizes and rates of the simulated myosin working stroke were estimated from the exponential fits. Box plots show the estimated parameters for each analysis method. Outliers are indicated by red dots. The substep sizes were estimated from both the time forward (f) and time reversed (r) ensemble averages. Horizontal dashed lines show the values of the simulated parameters. Unlike with **Fig. 5**, the time reversed averages generated from simulations with slower kinetics offer accurate estimates of the size of substep 1.

| Method | Average # of correctly detected interactions (mean ± SD) | Average # of missed interactions (mean ± SD) | # of false positive interactions / 100 seconds (mean ± SD) |
|---|---|---|---|
| **Single threshold** | 80 ± 4 | 20 ± 4 | 4 ± 1 |
| **Peak-to-peak** | 65 ± 5 | 36 ± 5 | 0 |

**Table S1. Detection of binding interactions using either the single or peak-to-peak covariance threshold method.** Average number of correctly identified binding interactions and frequency of false positive binding interactions detected with the single threshold method and peak-to-peak method for 10 data sets, each containing 100 simulated binding interactions (sets 1-10). Calculated values were rounded to the nearest whole number.

| Method | Error in binding initiation times (ms, mean with 95% CI) | Error in binding termination times (ms, mean with 95% CI) |
|---|---|---|
| **Single threshold** | 28.2 (+13.8, -21.7) | -28.6 (+19.1, -11.9) |
| **Peak-to-peak** | -55.5 (+69.0, -195.5) | 50.4 (+188.1, -64.9) |
| **Change point algorithm** | 0.5 (+9.0, -5.5) | 0.7 (+4.8, -4.2) |

**Table S2. The change point algorithm minimizes the error when detecting the locations of transitions.** Mean and 95% confidence intervals for the error when detecting transitions within simulated data sets 1-10 with the single threshold method, the peak-to-peak method, and the change point algorithm. When estimating the binding initiation times, 645 of 1000 transitions were detected and analyzed for the peak-to-peak method, 598 transitions were detected and analyzed for the single threshold method, and 644 transitions were detected and analyzed for the change point algorithm. The same number of transitions were detected and analyzed for each method when estimating the binding termination times. Note that a negative average error indicates that the detected transitions occurred before the actual transitions, on average.

| Time forward ensemble averages (mean with 95% CI) | | | | | |
|---|---|---|---|---|---|
| **Parameter** | **real** | **PTP** | **ST** | **PTP, CP** | **ST, CP** |
| **Substep 1 (nm)** | 4.7 (+0.4, -0.4) | 0.6 (+0.7, -0.5) p < 0.001 | 6.3 (+0.3, -0.3) p < 0.001 | 5.0 (+0.5, -0.3) p = 0.021 | 5.0 (+0.4, -0.6) p = 0.045 |
| **Substep 2 (nm)** | 1.7 (+0.5, -0.4) | 5.6 (+1.7, -0.8) p < 0.001 | 0.5 (+1.7, -0.4) p = 0.003 | 1.6 (+0.3, -0.4) p = 0.427 | 1.5 (+0.5, -0.6) p = 0.186 |
| **Total step (nm)** | 6.4 (+0.2, -0.2) | 6.2 (+2.0, -1.1) p = 0.026 | 6.8 (+2.1, -0.3) p = 0.002 | 6.6 (+0.1, -0.1) p = 0.001 | 6.5 (+0.2, -0.2) p = 0.186 |
| **Rate ($s^{-1}$)** | 68.7 (+15.8, -20. 9) | 20.2 (+7.4, -12.8) p < 0.001 | 84.3 (+43.8, -84. 3) p = 0.141 | 64.5 (+30.0, -20. 9) p = 0.473 | 63.6 (+42.3, -25. 0) p = 0.241 |
| **Time reversed ensemble averages (mean with 95% CI)** | | | | | |
| **Parameter** | **real** | **PTP** | **ST** | **PTP, CP** | **ST, CP** |
| **Substep 1 (nm)** | 5.7 (+0.2, -0.3) | 1.7 (+0.8, -0.4) p < 0.001 | 5.2 (+1.8, -5.2) p = 0.026 | 5.7 (+0.4, -0.6) p = 0.970 | 5.0 (+1.0, -5.0) p = 0.385 |
| **Substep 2 (nm)** | 0.7 (+0.2, -0.2) | 7.1 (+1.7, -1.4) p < 0.001 | 1.4 (+5.2, -1.4) p = 0.038 | 1.0 (+0.5, -0.4) p = 0.026 | 1.6 (+4.8, -1.1) p = 0.045 |
| **Total step (nm)** | 6.5 (+0.1, -0.2) | 8.8 (+1.4, -1.6) p < 0.001 | 6.6 (+0.4, -0.1) p = 0.003 | 6.7 (+0.1, -0.1) p < 0.001 | 6.7 (+0.4, -0.2) p = 0.011 |
| **Rate ($s^{-1}$)** | 4.3 (+2.2, -1.9) | 3.3 (+1.2, -0.6) p = 0.054 | 1.7 (+4.8 -1.7) p = 0.038 | 3.3 (+3.9, -2.0) p = 0.089 | 3.0 (+3.8, -2.9) p = 0.076 |

**Table S3. The change point algorithm improves ensemble averages.** 10 sets of data were simulated, each containing 100 binding interactions (sets 1-10). Interactions were detected using either the peak-to-peak or the single threshold method, and interactions were aligned using either the transitions estimated by the covariance threshold method or the change points identified by the change point algorithm. For each data set, ensemble averages were generated using either the known locations of actual simulated binding interactions (real) or using the binding interactions detected by each method of analysis.

The averages were fit with exponential functions, and the substep sizes and rates of the simulated myosin working stroke were estimated from the rates and amplitudes of the exponential fits. (top) Mean and 95% confidence intervals for the size of substep 1, the size of substep 2, the total step size, and the rate of transitioning from the first substep to the second substep, as estimated by the time forward ensemble averages. (bottom) Mean and 95% confidence intervals for the size of substep 1, the size of substep 2, the total step size, and the rate of transitioning from the second substep to the detached state, as estimated by the time reversed ensemble averages. The p-value for a given set of parameter values estimated by a given analysis method was obtained from the Wilcoxon rank sum test between those estimated parameter values and the values estimated by using the known locations of actual simulated binding interactions (real).

## Supporting References


1. Molloy, J. E., J. E. Burns, J. Kendrick-Jones, R. T. Tregear, and D. C. White. 1995. Movement and force produced by a single myosin head. Nature 378:209-212.
2. Mehta, A. D., J. T. Finer, and J. A. Spudich. 1997. Detection of single-molecule interactions using correlated thermal diffusion. Proceedings of the National Academy of Sciences of the United States of America 94:7927-7931.
3. Greenberg, M. J., H. Shuman, and E. M. Ostap. 2017. Measuring the Kinetic and Mechanical Properties of Non-processive Myosins Using Optical Tweezers. Methods Mol Biol 1486:483-509.
4. Laakso, J. M., J. H. Lewis, H. Shuman, and E. M. Ostap. 2008. Myosin I can act as a molecular force sensor. Science 321:133-136.
5. Chen, C., M. J. Greenberg, J. M. Laakso, E. M. Ostap, Y. E. Goldman, and H. Shuman. 2012. Kinetic schemes for post-synchronized single molecule dynamics. Biophysical journal 102:L23-25.
6. Greenberg, M. J., H. Shuman, and E. M. Ostap. 2014. Inherent force-dependent properties of beta-cardiac myosin contribute to the force-velocity relationship of cardiac muscle. Biophysical journal 107:L41-L44.
7. Sung, J., S. Nag, K. I. Mortensen, C. L. Vestergaard, S. Sutton, K. Ruppel, H. Flyvbjerg, and J. A. Spudich. 2015. Harmonic force spectroscopy measures load-dependent kinetics of individual human beta-cardiac myosin molecules. Nat Commun 6:7931.
8. Woody, M. S., M. J. Greenberg, B. Barua, D. A. Winkelmann, Y. E. Goldman, and E. M. Ostap. 2018. Positive cardiac inotrope omecamtiv mecarbil activates muscle despite suppressing the myosin working stroke. Nat Commun 9:3838.
9. Deacon, J. C., M. J. Bloemink, H. Rezavandi, M. A. Geeves, and L. A. Leinwand. 2012. Identification of functional differences between recombinant human alpha and beta cardiac myosin motors. Cellular and molecular life sciences : CMLS 69:2261-2277.
10. Sung, J., S. Sivaramakrishnan, A. R. Dunn, and J. A. Spudich. 2010. Single-molecule dual-beam optical trap analysis of protein structure and function. Methods in enzymology 475:321-375.
11. Takagi, Y., E. E. Homsher, Y. E. Goldman, and H. Shuman. 2006. Force generation in single conventional actomyosin complexes under high dynamic load. Biophysical journal 90:1295-1307.
12. Barrick, S. K., S. R. Clippinger, L. Greenberg, and M. J. Greenberg. 2019. Computational Tool to Study Perturbations in Muscle Regulation and Its Application to Heart Disease. Biophysical journal 116:2246-2252.
13. Clippinger, S. R., P. E. Cloonan, L. Greenberg, M. Ernst, W. T. Stump, and M. J. Greenberg. 2019. Disrupted mechanobiology links the molecular and cellular phenotypes in familial dilated cardiomyopathy. Proceedings of the National Academy of Sciences of the United States of America 116:17831-17840.
14. Greenberg, M. J., T. Lin, Y. E. Goldman, H. Shuman, and E. M. Ostap. 2012. Myosin IC generates power over a range of loads via a new tension-sensing mechanism. Proceedings of the National Academy of Sciences of the United States of America 109:E2433-2440.